J. Fluid Mech. (1970), *vol.* 43, *part* 1, *pp.* 187–209
Printed in Great Britain

Three-dimensional boundary layer near the plane of symmetry of a spheroid at incidence

By K. C. WANG

Research Institute for Advanced Studies, Baltimore, Maryland

(Received 17 October 1969)

This paper presents incompressible laminar boundary-layer results on both the leeside and windside of a prolate spheroid. The results are obtained by an implicit finite difference method of the Crank–Nicolson type. Particular attention has been given to the determination of separation and of embedded streamwise vortices. No restriction on the angle of attack or the thickness ratio is imposed, nor are there invoked any of the common assumptions such as similarity, conical flow and others. The results suggest an embedded vortex region existing between the regular boundary-layer region and the separated region. At higher angle of attack, the vortex region becomes so thick that it itself may be more appropriately called 'separated' also. The latter possibility leads to questions of applicability for existing theories on three-dimensional separation.

1. Introduction

The three-dimensional boundary layer near the plane of symmetry for the case of a supersonic cone at large angle of attack was first investigated by Moore (1952, 1953). On the windside, Moore's solutions show the expected thinning of a boundary layer as the angle of attack is increased. On the leeside, numerical solutions were difficult to obtain. Asymptotic analysis indicated that unique solutions are limited to small angles of attack, and beyond a certain angle, the solutions do not exist at all. This clearly reflects the fact that the flow over a cone separates along a generator; beyond a certain angle of attack, the leeside of a symmetry plane lies completely inside the separated region and hence no boundary-layer solution can be expected.

Moore further sketched without proof the formation of vortices which remain embedded inside a thin boundary layer (figure 1(*a*)). At still larger angle of attack, he depicted that the boundary layer exhibits a crosswise separation (figure 1(*b*)) on the leeside similar to the familiar flow pattern around a circular cylinder.

Moore's cone problem has later been extended to include heat transfer, mass transfer and other features, but consideration was invariably confined to the windside. Trella & Libby (1965) investigated some similar solutions near the symmetry plane in the hypersonic limit. Otherwise little progress has been made with respect to the basic nature of especially the leeside flow of body shapes other than a cone at large angle of attack.

In a related work, Nonweiler (1955) considered the boundary layer over a slender body of revolution at small angle of attack. He separated the boundary layer into axial- and cross-flow parts, and carried out the cross-flow part only. The significance of such a cross-flow approach is naturally very limited. Nevertheless, his calculations showing the embedded vortices are interesting. The embedded vortices were also implied in a work by Martin & Greber (1957) on the boundary layer over the cylindrical portion of slender bodies of revolution at small angles of attack. Their method of approach, however, is subject to similar shortcomings to Nonweiler's.

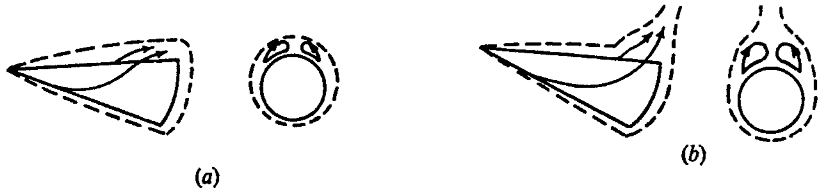

Figure 1. Cone at angle of attack.

In the present work, a finite-difference method is used to calculate exactly the boundary layer near the symmetry plane of a prolate spheroid. Both the angle of attack and the thickness ratio are arbitrary. This problem is chosen because (i) it is critically subject to the cross flow, (ii) the body shape is of considerable practical interest and (iii) the corresponding inviscid flow is exactly known. Numerical solutions have been obtained for both the windside and the leeside at different angles of attack. Particular attention has been given to the determination of separation and of embedded streamwise vortices. In contrast to Moore's work, we have encountered no particular difficulty in obtaining the leeside solutions. The present results not only partially confirm the depiction shown in figures 1(*a*), (*b*) but provide further details of the flow structure. Although this work is limited to incompressible flow, it is otherwise free from all common restrictions such as conical properties, similarity, slender body, and small angle of attack.

The symmetry-plane solutions obtained are of considerable interest for several reasons. They are exact solutions and relatively easy to obtain. They are the most important parts of the complete solutions over an entire body, and frequently are all one would need for practical purposes. Knowing these symmetry-plane solutions, a fairly clear picture of the complete flow immediately follows. Since these solutions are exact solutions, they can also be used to check other three-dimensional calculations.

The boundary layer over a slender spheroid at small angle of attack was considered by Eichelbrenner & Oudart (1955). They used the integral method plus the approximation of the independence principle. Since the point of interest and the method of approach are so different from those of the present work, little meaningful comparison can be made despite the fact that the body shape in both cases is a spheroid.

2. Formulation of the problem

The inviscid solution

A prolate spheroid (also known as the ovary spheroid) is an ellipsoid of revolution about the major axis of an ellipse. The inviscid flow potential over a prolate spheroid is known exactly (see Lamb 1932). For our present purpose, we need to be concerned only with the surface potential which may be put in terms of two surface co-ordinates μ and θ (figure 2). μ $(-1 \leqslant \mu \leqslant +1)$ is constant along the parallels and θ is constant along the meridians. The corresponding metric coefficients h_μ and h_θ are given by

$$h_\mu = \left[\frac{1-e^2\mu^2}{1-\mu^2}\right]^{\frac{1}{2}}, \tag{1a}$$

$$h_\theta = [(1-e^2)(1-\mu^2)]^{\frac{1}{2}} = r, \tag{1b}$$

where the eccentricity $$e = [1-(b^2/a^2)]^{\frac{1}{2}}, \tag{1c}$$

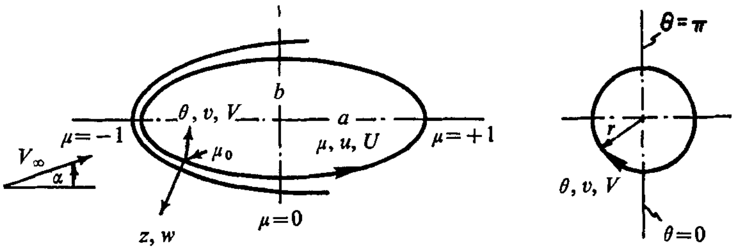

FIGURE 2. Spheroid.

a and b are the semi-major and semi-minor axes of the spheroid, r is the cross-sectional radius. With the free stream V_∞ at an angle of attack α (with the plane $\theta = 90°$), the non-dimensionalized (with respect to $V_\infty a$) surface potential, ϕ, consists of an axial (along the major axis) part and a cross-part

$$\phi = [(1+k_a)(\cos\alpha)\mu - (b/a)(1+k_c)(\sin\alpha)(1-\mu^2)^{\frac{1}{2}}\cos\theta], \tag{2}$$

where k_a and k_c are known as the axial and cross-coefficients of virtual mass and are defined by

$$k_a = \left[\frac{1}{2e}\log\frac{1+e}{1-e} - 1\right] \Big/ \left[\frac{1}{1-e^2} - \frac{1}{2e}\log\frac{1+e}{1-e}\right], \quad k_c = \frac{1}{1+2k_a}. \tag{2a,b}$$

It follows from (2) that the non-dimensionalized surface pressure

$$2(p-p_\infty) = 1 - \left\{\left[\frac{(1+k_a)(\cos\alpha)[1-\mu^2]^{\frac{1}{2}} + (b/a)(1+k_c)(\sin\alpha)\mu\cos\theta}{[1-e^2\mu^2]^{\frac{1}{2}}}\right]^2 \right.$$
$$\left. + [(1+k_c)\sin\alpha\sin\theta]^2\right\}. \tag{3}$$

Boundary-layer problem

To study the boundary layer near the plane of symmetry, we continue to use the co-ordinates μ, θ plus the normal (to the body surface) co-ordinate z, but the origin is located at the stagnation point $\mu = \mu_0$. We denote by u, v, w the velocities along the μ, θ and z directions, and by U and V the inviscid velocities at the edge of the boundary layer in the μ and θ directions.

z is made dimensionless with $a/R^{\frac{1}{2}}$, where $R\ (= V_\infty a/\nu)$ is the Reynolds number, ν the kinematic viscosity. u, v, U and V are non-dimensionalized with V_∞, w with $V_\infty/R^{\frac{1}{2}}$, pressure p with ρV_∞^2 where ρ is the density.

At the plane of symmetry, $\theta = 0$ and π, one has

$$v = \partial v/\partial\mu = \partial v/\partial z = \partial^2 v/\partial z^2 = V = \partial V/\partial\mu = 0, \tag{4a}$$

$$\partial u/\partial\theta = 0, \quad \partial p/\partial\theta = 0. \tag{4b, c}$$

With those quantities vanishing, the entire θ-momentum equation becomes identically zero, while the continuity and μ-momentum equations take the form

$$\frac{\partial(ru)}{rh_\mu\partial\mu}+\frac{1}{r}\frac{\partial v}{\partial\theta}+\frac{\partial w}{\partial z} = 0, \tag{5a}$$

$$\frac{u}{h_\mu}\frac{\partial u}{\partial\mu}+w\frac{\partial u}{\partial z} = -\frac{1}{h_\mu}\frac{\partial p}{\partial\mu}+\frac{\partial^2 u}{\partial z^2}. \tag{5b}$$

Equations (5*a*, *b*) differ from those for axisymmetrical boundary layers only in the presence of $(1/r)\,\partial v/\partial\theta$ which is not negligible[†] compared to the other two terms in the continuity equation. $\partial v/\partial\theta$ may be determined from an equation[‡] obtained by differentiating (see Moore 1953) the original θ-momentum equation, i.e.

$$\frac{u}{h_\mu}\frac{\partial}{\partial\mu}\left(\frac{\partial v}{\partial\theta}\right)+w\frac{\partial}{\partial z}\left(\frac{\partial v}{\partial\theta}\right)+\frac{1}{r}\left(\frac{\partial v}{\partial\theta}\right)^2+\frac{u}{h_\mu}\frac{\partial r}{\partial\mu}\frac{1}{r}\frac{\partial v}{\partial\theta} = -\frac{1}{r}\frac{\partial^2 p}{\partial\theta^2}+\frac{\partial^2}{\partial z^2}\left(\frac{\partial v}{\partial\theta}\right). \tag{5c}$$

Thus there are three equations for three unknowns, u, $\partial v/\partial\theta$ and w, with two independent variables, μ and z. u is indirectly affected by v through w. In contrast, u, v and w are mutually coupled in the full three-dimensional case. The pressure gradients are found from (3)

$$-\frac{\partial p}{h_\mu\partial\mu} = \frac{(1+k_a)^2\cos^2\alpha}{(1-e^2\mu^2)^{\frac{3}{2}}}\left([1-\mu^2]^{\frac{1}{2}}\pm\lambda\mu\right)\left[\left(-\mu\pm\lambda[1-\mu^2]^{\frac{1}{2}}\right)\right.$$
$$\left.+\frac{e^2\mu}{1-e^2\mu^2}\left(1-\mu^2\pm\lambda\mu[1-\mu^2]^{\frac{1}{2}}\right)\right], \tag{5d}$$

$$-\frac{\partial^2 p}{\partial\theta^2} = \frac{1}{(b/a)}(1+k_a)(1+k_c)\cos\alpha\sin\alpha\left[\lambda-\left(\frac{b}{a}\right)^2\frac{(\pm\mu)}{1-e^2\mu^2}\left([1-\mu^2]^{\frac{1}{2}}\pm\lambda\mu\right)\right], \tag{5e}$$

where the sign ± implies that the plus is for $\theta = 0$ and the minus is for $\theta = \pi$ and

$$\lambda = \left(\frac{b}{a}\right)\frac{(1+k_c)\sin\alpha}{(1+k_a)\cos\alpha}. \tag{5f}$$

[†] This in fact is a strong point against the small cross-flow approximation. Along a streamline, even though the cross-velocity v is small, the cross-derivative of v is not necessarily small.

[‡] The same can be arrived at by a perturbation procedure (Squire 1955). Let

$$u = u_0+\theta u_1+\ldots,\quad v = \theta v_1+\ldots,\quad w = w_0+\theta w_1+\ldots,\quad p = p_0+\tfrac{1}{2}\theta^2 p_1+\ldots;$$

then the equations for u_0, v_1, w_0 and p_1 are just (5*a*, *b*, *c*).

The boundary conditions are

$$u = U, \quad \partial v/\partial\theta = \partial V/\partial\theta \quad \text{as} \quad z \to \infty, \tag{6a}$$

$$u = \partial v/\partial\theta = w = 0 \quad \text{at} \quad z = 0, \tag{6b}$$

$$u = 0 \quad \text{at} \quad \mu = \mu_0, \tag{6c}$$

where U and $\partial V/\partial\theta$ can be found from (2)

$$U = \frac{1}{[1-e^2\mu^2]^{\frac{1}{2}}}[(1+k_a)(\cos\alpha)[1-\mu^2]^{\frac{1}{2}} + (b/a)(1+k_c)(\sin\alpha)\mu\cos\theta], \tag{6d}$$

$$\partial V/\partial\theta = (1+k_c)\sin\alpha\cos\theta. \tag{6e}$$

The crosswise skin friction vanishes (since $\partial v/\partial z = 0$) at the plane of symmetry, the total skin friction c_f is therefore just the streamwise skin friction defined by

$$c_f = \frac{\text{shearing stress}}{\rho V_\infty^2} = \frac{1}{R^{\frac{1}{2}}}\left(\frac{\partial u}{\partial z}\right)_{z\to 0}, \tag{7a}$$

where R is the free-stream Reynolds number $(V_\infty a/\nu)$.

General three-dimensional separation has not been undisputedly defined; but at the plane of symmetry, the separation point is usually determined by the vanishing of the streamwise skin friction, i.e. by $\partial u/\partial z \to 0$ as $z \to 0$. The significance of an analogous term, namely $\partial(\partial v/\partial\theta)/\partial z \to 0$ as $z \to 0$, will be discussed later.

The outer edge of the boundary layer is determined by the condition of smooth transition of both u and $\partial v/\partial\theta$ profiles, i.e. $\partial u/\partial z$ and $\partial(\partial v/\partial\theta)/\partial z = 0$ as $z \to \infty$.

The displacement and momentum thicknesses in non-dimensionalized form are

$$\Delta^* = \int_0^\infty \left(1 - \frac{u}{U}\right) dz, \tag{7b}$$

$$\theta^* = \int_0^\infty \frac{u}{U}\left(1 - \frac{u}{U}\right) dz. \tag{7c}$$

3. Difference method of solution

The type of problem formulated in §2 has previously been solved for the similarity case or by series expansion. The similar solution is rather restrictive; the series solution has a limited range of validity and hence is not suitable to determine the separation point. We choose to obtain exact numerical solutions by a Crank–Nicolson type finite-difference method similar to those for two-dimensional and axisymmetrical cases (see, for example, Flügge–Lotz & Blottner 1963).

The boundary layer on the windside ($\theta = 0$) or the leeside ($\theta = \pi$) is resketched in figure 3. We divide the region of interest by a mesh and denote the location of a point by index l and n according to

$$\mu = \mu_i + l\Delta\mu \quad (l = 0, 1, 2, \ldots),$$

$$z = n\Delta z \quad (n = 0, 1, 2, \ldots, N+1),$$

where $\mu = \mu_i$ is the initial-value line along which flow conditions are known, say, from the stagnation-point solution. N is a finite suitably-chosen number of divisions across the boundary layer. The problem becomes specifically to determine solutions at station $l+1$ assuming the solutions at station l are known. Each term of the differential equation is approximated by a difference quotient around a central point.

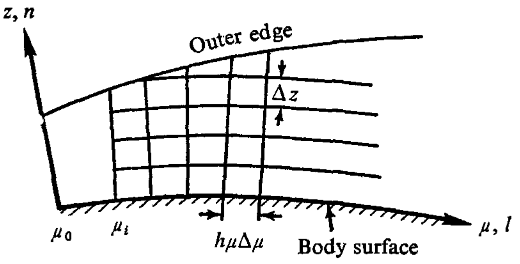

FIGURE 3. Difference mesh.

Figure 4 (a) shows the mesh for a single calculation of the momentum equations. Typical quotients are

$$\left(\frac{\partial(\ )}{\partial\mu}\right)_{l+\frac{1}{2},n} = \frac{(\ )_{l+1,n}-(\ )_{l,n}}{\Delta\mu}+O(\Delta\mu)^2, \tag{8a}$$

$$\left(\frac{\partial(\ )}{\partial z}\right)_{l+\frac{1}{2},n} = \frac{(\ )_{l+1,n+1}-(\ )_{l+1,n-1}+(\ )_{l,n+1}-(\ )_{l,n-1}}{4\Delta z}+O(\Delta z)^2+O(\Delta\mu)^2, \tag{8b}$$

$$\left(\frac{\partial^2(\ )}{\partial z^2}\right)_{l+\frac{1}{2},n} = \frac{1}{2(\Delta z)^2}[(\delta^2(\ ))_{l+1,n}+(\delta^2(\ ))_{l,n}]+O(\Delta z)^2+O(\Delta\mu)^2, \tag{8c}$$

where
$$(\delta^2(\ ))_{l+1,n} = (\ )_{l+1,n+1}-2(\ )_{l+1,n}+(\ )_{l+1,n-1}.$$

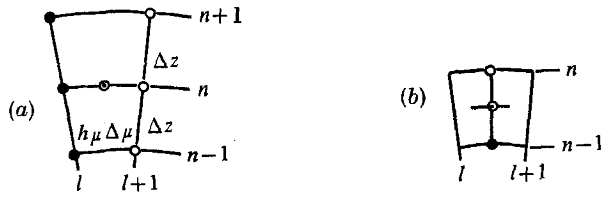

FIGURE 4. Mesh for a single calculation. (a) For momentum equations. (b) For continuity equation. ●, solutions known; ○, solution to be calculated; ⊙, central point.

With those quotients substituted into ($5b, c$), one obtains two difference momentum equations

$$a_{1n}u_{l+1,n-1}+b_{1n}u_{l+1,n}+c_{1n}u_{l+1,n+1} = d_{1n}, \tag{9a}$$

$$a_{2n}(\partial v/\partial\theta)_{l+1,n-1}+b_{2n}(\partial v/\partial\theta)_{l+1,n}+c_{2n}(\partial v/\partial\theta)_{l+1,n+1} = d_{2n}, \tag{9b}$$

where the coefficients $a_{1n}, b_{1n}, \ldots, a_{2n}, \ldots$ are given in appendix A. Equations ($9a, b$) can be solved in the form of a tridiagonal matrix by well-known procedures (for example, Forsyth & Wasow 1960) to determine u and $\partial v/\partial\theta$ at $l+1$.

The continuity equation is used to determine w explicitly in both the z direction and μ direction (figure 4(*b*)). Furthermore, w is evaluated at $l+\frac{1}{2}$ instead of $l+1$. The derivatives are approximated by

$$\left(\frac{\partial w}{\partial z}\right)_{l+\frac{1}{2},\,n-\frac{1}{2}} = \frac{w_{l+\frac{1}{2},\,n} - w_{l+\frac{1}{2},\,n-1}}{\Delta z}, \tag{10a}$$

$$\left(\frac{\partial u}{\partial \mu}\right)_{l+\frac{1}{2},\,n-\frac{1}{2}} = \frac{u_{l+1,\,n} - u_{l,\,n} + u_{l+1,\,n-1} - u_{l,\,n-1}}{2\Delta\mu}. \tag{10b}$$

Substituting into (5*a*) yields

$$w_{l+\frac{1}{2},\,n} = w_{l+\frac{1}{2},\,n-1} - d_{3n}, \tag{10c}$$

where d_{3n} is given in appendix A.

The iteration procedures are similar to those familiar for the two-dimensional case, and no detailed descriptions are necessary. Integration is stopped in the calculations whenever the successive values differ less than a half percent of the value of the preceding cycle. To evaluate the skin friction, the derivative $\partial u/\partial z$ is approximated by a four-point Newton's forward differentiation formula, i.e.

$$\left(\frac{\partial u}{\partial z}\right)_{n=0} = \frac{1}{6\Delta z}\left(2u_{n=3} - 9u_{n=2} + 18u_{n=1} - 11u_{n=0}\right). \tag{11a}$$

To test the boundary-layer outer-edge condition of smooth transition, i.e. $\partial f/\partial z = 0$, we set

$$\left|\,|f_{l+1,N+1}| - |f_{l+1,N}|\,\right| < \epsilon, \tag{11b}$$

where f is either u or $\partial v/\partial\theta$ and ϵ is a prescribed small number. In the present calculations, ϵ is taken to be a half percent of $f_{l+1,N}$. As μ increases, the boundary layer grows thicker; one or more points in the z direction must be added at station $l+1$ in order to ensure the smooth transition. Addition of too many points at a particular μ station indicates that $\Delta\mu$ is too large. In the present calculations, $\Delta\mu$ is reduced whenever more than one point (in the z direction) needs to be added.

The initial values needed for starting the present calculations were obtained by solving the three-dimensional stagnation-point boundary-layer equations of Howarth (1951) and Squire (1955). Application of their method to the present case is summarized in appendix B.

Consistency of the present difference scheme follows from the condition that the truncation errors vanish with the step sizes. Linearized stability can be shown similar to that of the heat equation, and no instability difficulty has actually been experienced throughout the entire computation. Convergence is assessed from results obtained by reducing the step sizes.

4. Results

Numerical results have been obtained for the thickness ratio $b/a = \frac{1}{4}$ and different values of the angle of attack α.

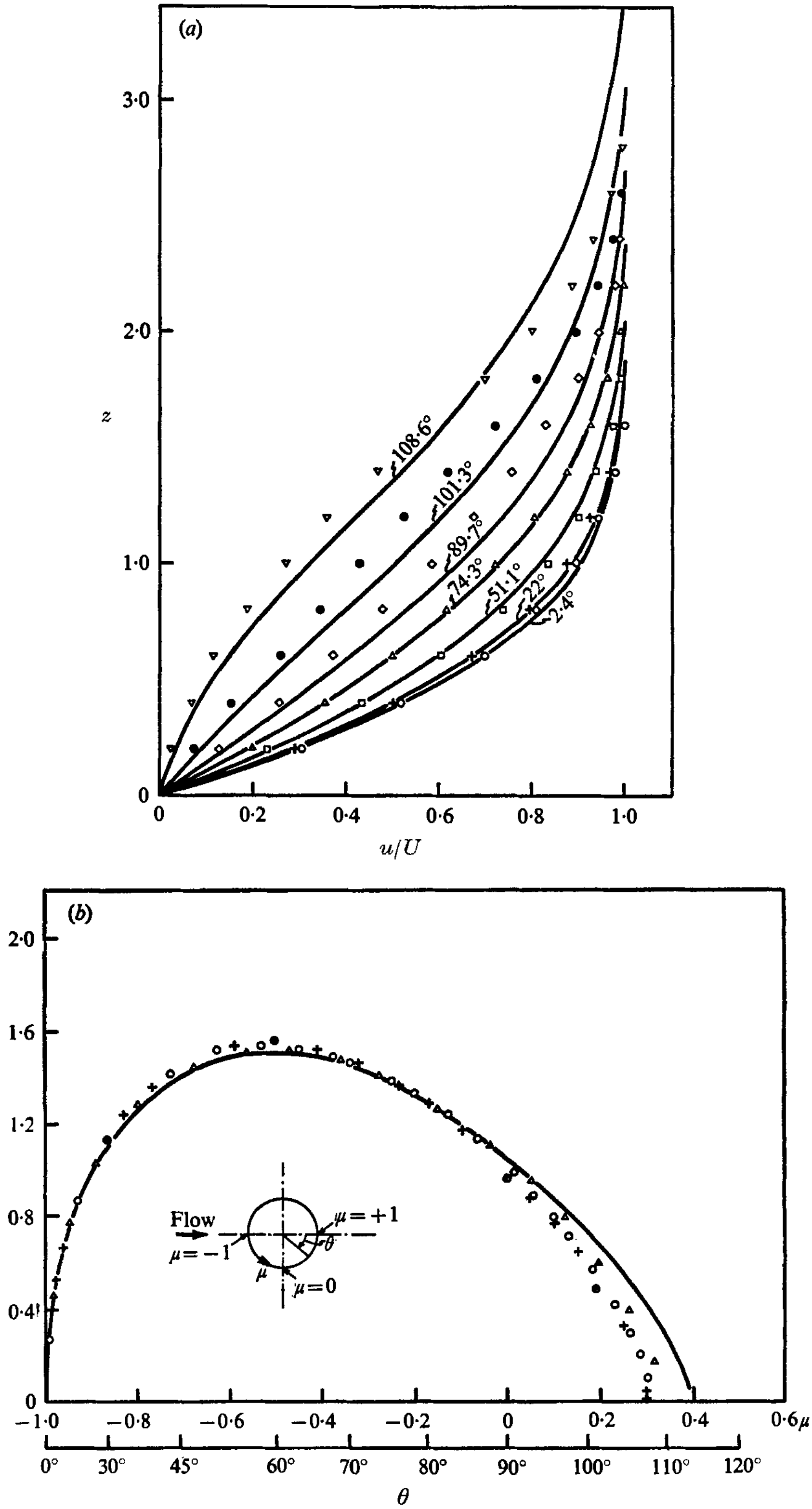

FIGURE 5. (*a*) u-velocity profile. ——, present ($\Delta\mu = 0{\cdot}0025$, $\Delta z = 0{\cdot}0816$). Schlichting: ○, 0°; +, 25°; □, 50°; △, 75°; ◇, 90°; ●, 100°; ▽, 109·6°. (*b*) Skin friction. Present: +, maximum step size $\Delta\mu = 0{\cdot}01$, $\Delta z = 0{\cdot}0816$; ○, 0·005, 0·0816; △, 0·0025, 0·0816; ——, 0·001, 0·0408. ⊙, Smith & Clutter.

Test case, sphere

The programme was first tested against some known results for a limiting case, sphere ($\alpha = 0$ and $b/a = 1$). Figure 5(*a*) shows the velocity profiles across the boundary layer compared with the series solutions according to best reading from figure 10·5 of Schlichting (1955). As expected, the series solution becomes poorer further downstream. Figure 5(*b*) gives the skin friction along the surface. As the step sizes become finer, the results converge gradually. Smith & Clutter's (1963) results are shown for comparison.

Windside results

Shown in figures 6(*a*)–(*f*) are the boundary-layer results on the windside ($\theta = 0$). Figures 6(*a*), (*b*) give the inviscid velocity U and pressure p. As the angle of attack increases, the u and p distribution become more asymmetrical. As far as the after-portion ($0 \leqslant \mu \leqslant 1$) is concerned, such asymmetry is beneficial because of the accelerating flow and favourable pressure gradient. Near the front end ($\mu = -1$), asymmetry results in sharp variations of the U velocity and pressure. The latter leads to, among other things, rapid changes of u-velocity profiles and the skin friction as will be seen later.

Figure 6(*c*) shows a few non-dimensionalized streamwise velocity profiles, u/U, across the boundary layer. In general these profiles are similar to those for two-dimensional cases. As expected, the boundary-layer thickness decreases as the angle of attack increases. This can be seen by comparing the outer edge z of the last μ station shown for each value of α.

Large changes of the u profile occur generally in two regions; one approaching the separation point, another near the front end. This can be seen, for example, from the fact that the profiles at $\mu = 0{\cdot}9286$ and $0{\cdot}9113$ for the case $\alpha = 12°$ are so apart in proportion to the interval in μ compared to the upstream results ($\mu \leqslant 0{\cdot}9113$). Such large change of u profile near the separation point is familiar, and the reason is the sharp increase of the boundary-layer thickness. But the same effect near the front end occurs for different reasons. It is due to rapid variations of the inviscid velocity and pressure; in fact the pressure gradient is favourable while the boundary-layer thickness grows very slowly.

At still larger angle of attack (say, $\alpha = 31{\cdot}87°$), the profiles do not always go up in the arrow direction (figure 6(*c*)) as μ increases. Instead the profiles first follow such a trend up to, say, $\mu = 0{\cdot}2044$; but then reverse until further downstream. This is why the profile for $\mu = 0{\cdot}2044$ falls between those for $\mu = 0{\cdot}9544$ and $\mu = 0{\cdot}9871$. This behaviour is connected to the downstream increase of the skin friction (figure 6(*e*)).

Figure 6(*d*) gives the profiles of non-dimensionalized $(\partial v/\partial\theta)/(\partial V/\partial\theta)$ across the boundary layer. Like the u-velocity profiles, the $\partial v/\partial\theta$ profiles also go up as μ increases. Particular attention here is called to the S-shaped profiles which occur. Implications of such profiles will be explained later. For the axisymmetrical case ($\alpha = 0$), $\partial v/\partial\theta$ is identical to zero. As α increases, S-shaped profiles gradually make their appearance just before separation. Further increase of α (say 12°) moves the separation point farther downstream, and at the meantime decreases the size of the S-loop. For still larger angle of attack ($\alpha = 31{\cdot}87^\circ$) no separation ever occurs on the windside, and the S-shaped $\partial v/\partial\theta$-profiles disappear.

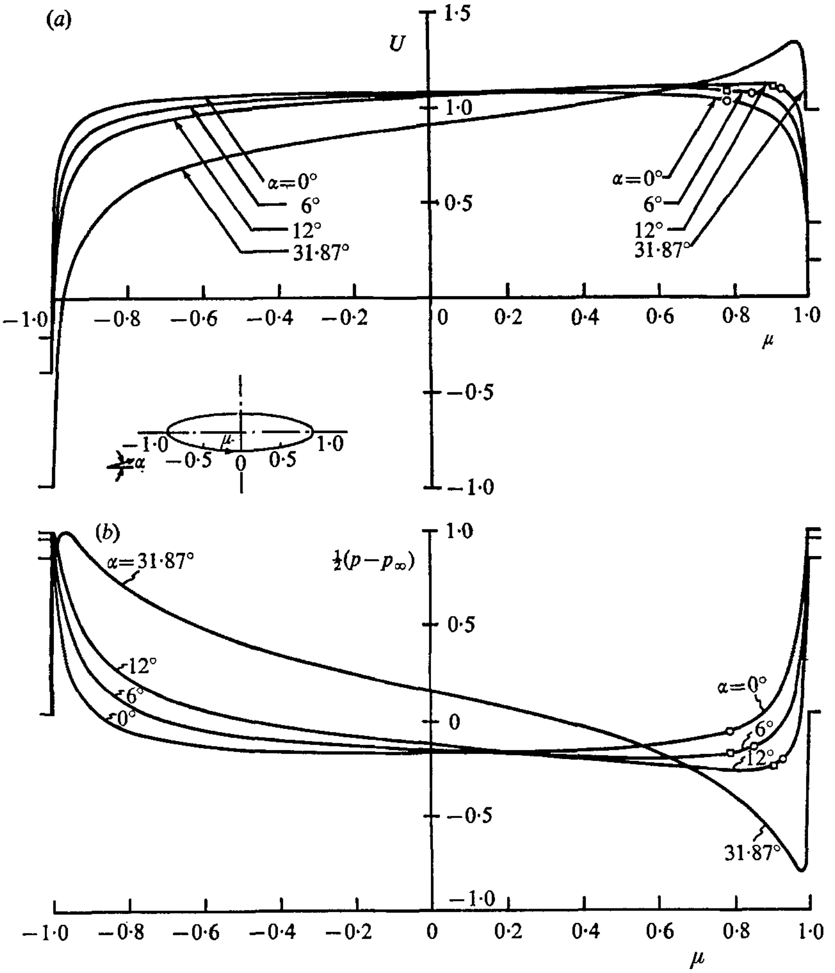

FIGURE 6(*a*) and (*b*). $b/a = \frac{1}{4}$, $\theta = 0$. ○, separation; □, start of vortex. (*a*) Inviscid velocity. (*b*) Pressure.

The skin-friction distributions are shown in figure 6(*e*). These are quite different from the familiar ones for a flat plate or a sphere (see figure 5(*b*)). For smaller angle of attack including $\alpha = 0$, the skin friction increases sharply from zero at the stagnation point to a maximum value and then decreases gradually and monotonically to zero at the separation point. For larger angle of attack (for example, $\alpha = 31{\cdot}87^\circ$), the skin friction first rapidly increases and then levels off for most of the flow. Toward the rear end, the skin friction resumes its sharp increase until a maximum is reached and suddenly drops thereafter.

Such variation of streamwise skin friction follows from the variation of u profile, particularly the part of the profile near the wall. For example, the increase of skin friction near the rear end (say $0{\cdot}7 \leqslant \mu \leqslant 0{\cdot}95$ for $\alpha = 31{\cdot}87^\circ$) is attributed to the fact that the u profiles there shift downward instead of upward as μ

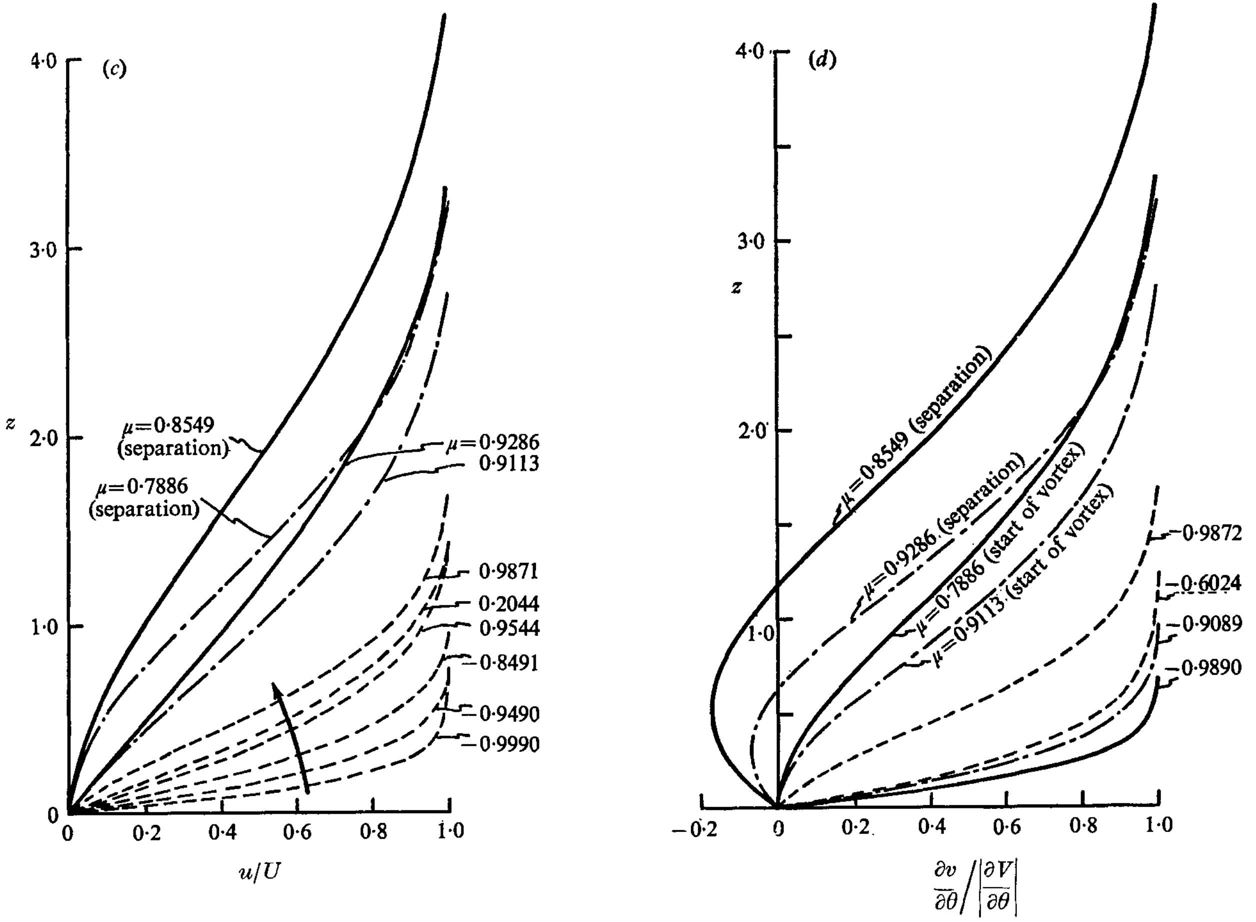

FIGURE 6 (c) and (d). $b/a = \frac{1}{4}$, $\theta = 0$. ——, $\alpha = 6°$; —·—, $\alpha = 12°$; - - -, $\alpha = 31{\cdot}87°$. (c) Streamwise velocity. (d) Lateral derivative of cross-velocity.

increases. Similarly the up-and-down behaviour of skin friction near the front end (for α between 0° and 12°), may be traced to the variation of u profile there. On the other hand, the variation of u profile is affected by the pressure. Hence once the pressure distribution is known, one can have a rough idea of the flow with the aid of typical existing solutions.

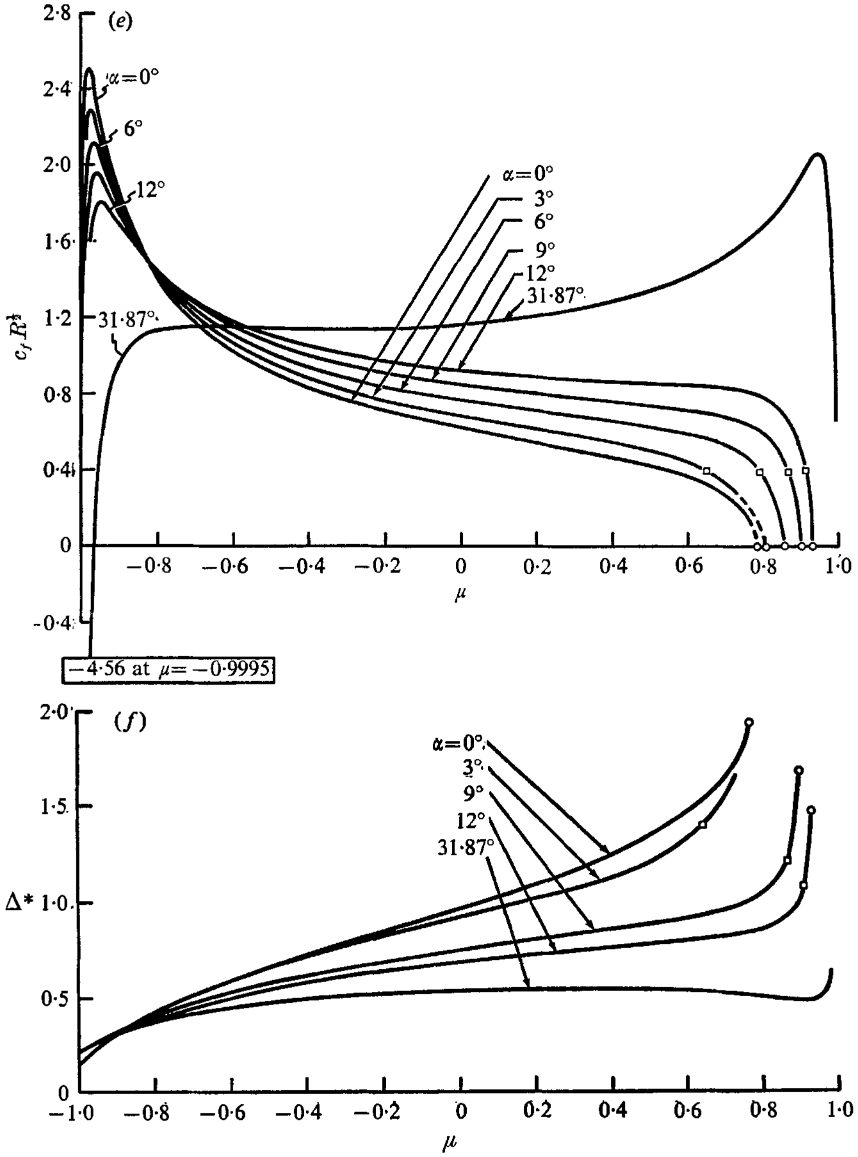

FIGURE 6(*e*) and (*f*). $b/a = \frac{1}{4}$, $\theta = 0$. ○, separation; □, start of vortex. (*e*) Skin friction. (*f*) Displacement thickness.

The point of vanishing skin friction is, by definition, the separation point. As the angle of attack increases, the separation point gradually moves downstream as expected. In actual computation, the approach to the separation point is accompanied by a small skin-friction value and extremely slow convergence of the iterations.

Figure 6(f) shows the displacement thickness. As expected, the integrated thickness becomes thinner as the angle of attack increases. When α is small or moderate, the monotonic increase of thickness is familiar. For large α (say 31·87°), the displacement thickness decreases over a certain interval downstream. This does not indicate the decrease of the actual outer edge of the boundary layer. Rather this reflects the reverse trend of the u profile (figure 6(c)) which shifts downward instead of upward as μ increases.

Leeside results

Results for the leeside ($\theta = \pi$) are shown in figures 7(a)–(f). As expected, the leeside boundary-layer thickness grows rapidly; many more steps are needed

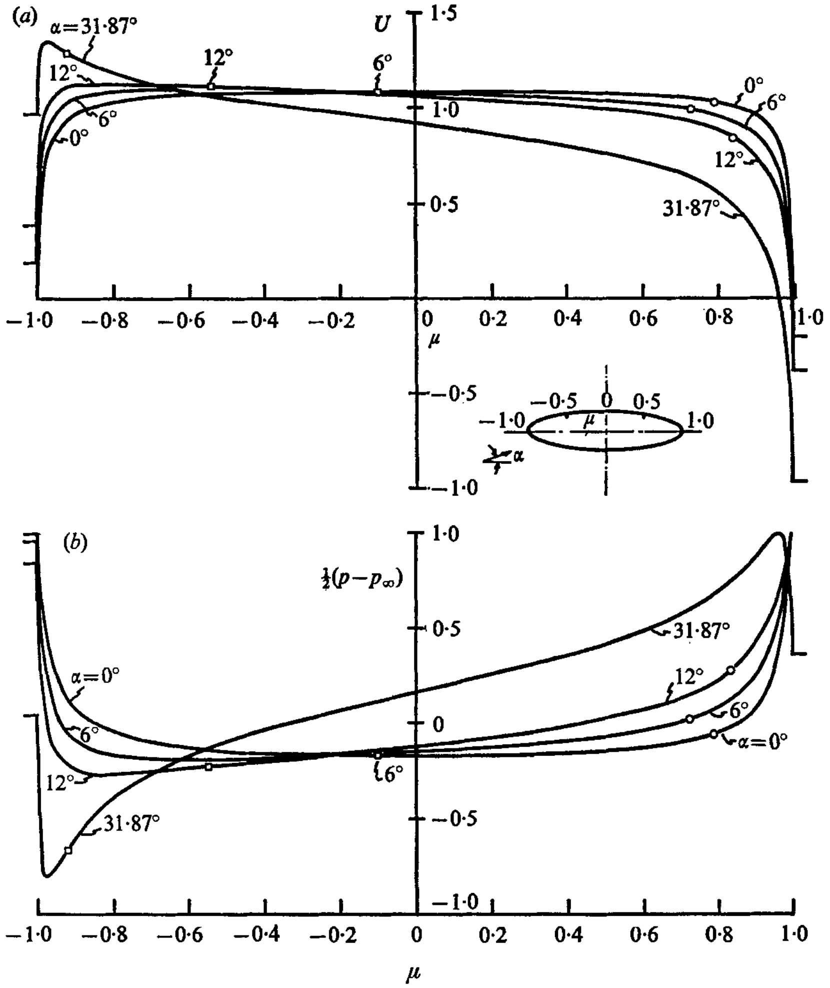

FIGURE 7(a) and (b). $b/a = \frac{1}{4}$, $\theta = \pi$. ○, separation; □, start of vortex. (a) Inviscid velocity. (b) Pressure.

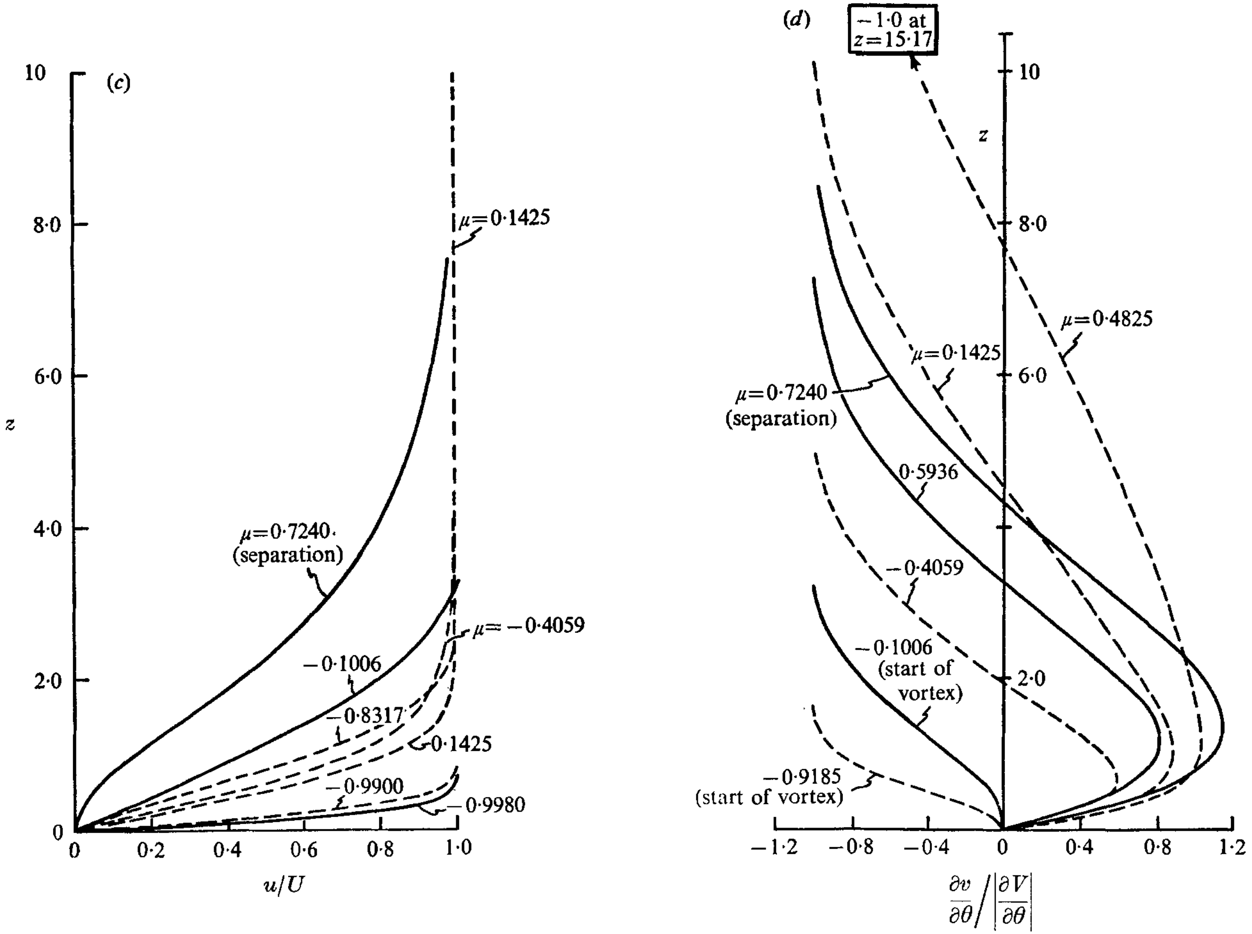

FIGURE 7(*c*) and (*d*). $b/a = \frac{1}{4}$, $\theta = \pi$. ——, $\alpha = 6°$; – – –, $\alpha = 31{\cdot}87°$. (*c*) Streamwise velocity. (*d*) Lateral derivative of cross-velocity.

along both streamwise and normal directions in order to continue the integration. But otherwise there was no particular difficulty with the calculation.

Figures 7(*a*), (*b*) give the inviscid velocity and pressure. In contrast to the

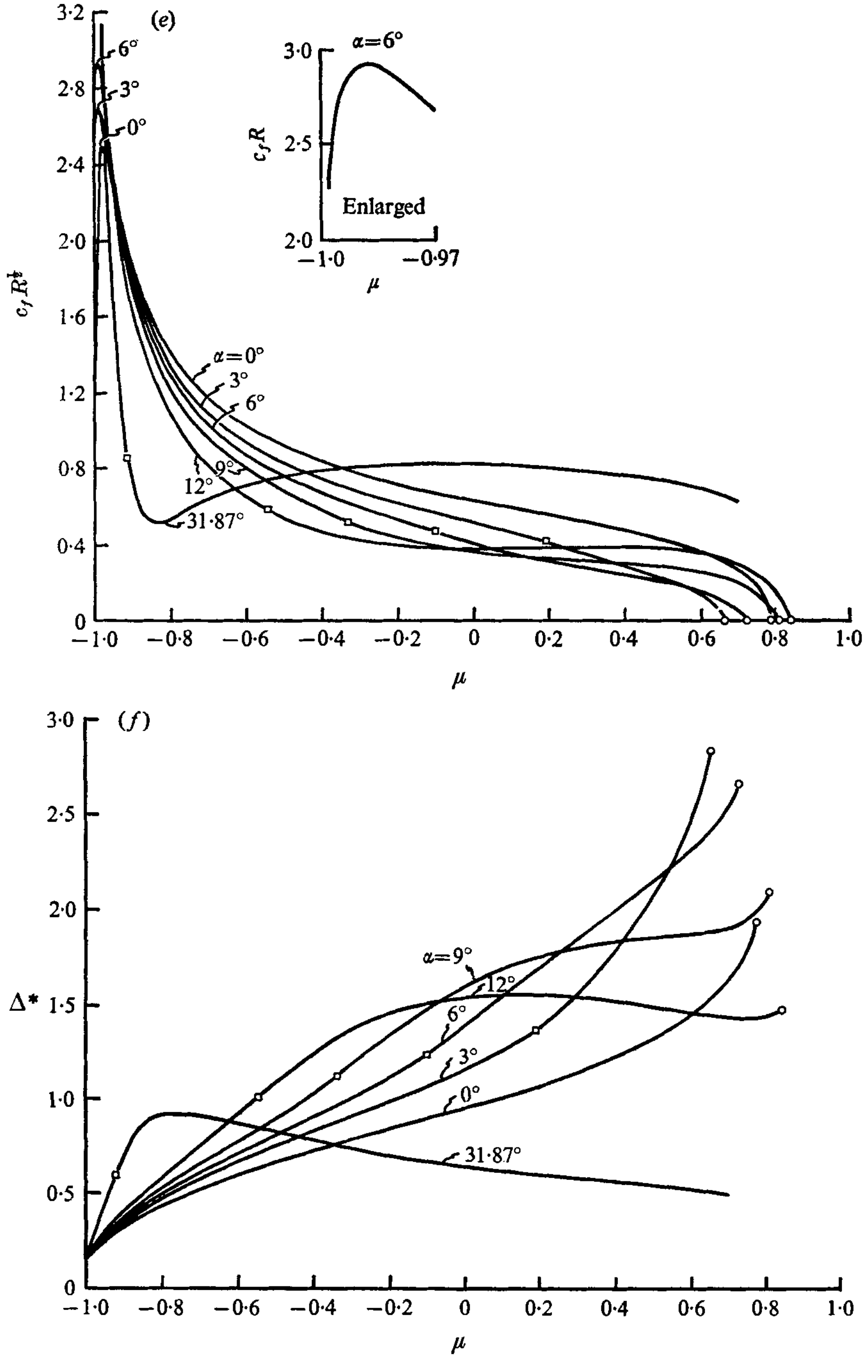

FIGURE 7(*e*) and (*f*). $b/a = \frac{1}{4}$, $\theta = \pi$. ○, separation; □, start of vortex. (*e*) Skin friction. (*f*) Displacement thickness.

windside, a large angle of attack now causes the flow to decelerate and the pressure gradient to be adverse along the entire leeside. These unfavourable conditions completely change the flow character.

For low angle of attack (say $\alpha = 6°$), the u-velocity profiles (figure 7 (*c*)) exhibit the same pattern as that prevailing on the windside. For larger angle of attack (say $\alpha > 12°$), the u profile behaves differently. While the outer edge distance increases rapidly in the downstream direction, the profiles remain nearly flat. Such nearly-flat u-velocity profiles lead to unusual features of the skin friction and displacement thickness to be shown later. The flow seems to become more like an inviscid uniform flow than a boundary layer, though near the front end ($\mu = -1$), the flow remains that of a thin boundary layer.

The cross derivative $\partial v/\partial \theta$ also changes considerably (figure 7 (*d*)). First of all, the S-shaped profile appears farther upstream even for relatively low angle of attach (say 3° and 6°). The higher the angle of attack is, the farther upstream such S-shaped profile emerges. Secondly, the loop region (note the scale difference compared with figure 6 (*d*)) becomes larger. In the z direction, the loop extends to almost half of the boundary layer. A larger loop implies a larger embedded vortex as will be explained later.

The skin-friction variations are shown in figure 7 (*e*). For all angles of attack, the skin friction increases sharply near the front end ($\mu = -1$). After reaching a maximum (see the enlarged plot) also near the front end, it decreases monotonically to zero for the cases of low angle of attack (say $\alpha = 3°$ or $6°$). Such behaviour is familiar on the windside. Increase of angle of attack, however, changes this pattern. The skin friction (for example, $\alpha = 31{\cdot}87°$) then first drops rapidly to a minimum (near $\mu = -0{\cdot}83$) and then increases before it finally resumes its decline. The presence of a minimum follows from the u-velocity profiles in figure 7 (*c*) which shows that the profile for $\mu = -0{\cdot}83$ has the smallest gradient $\partial u/\partial z$. The general inter-relations among the skin friction, u profile and pressure discussed in connection with figure 6 (*e*) hold here also.

More unusual are the separation results. Normally one would expect that the separation point moves farther upstream as the angle of attack increases. This expectation is true only in the case of the starting of the vortex, but not for the separation. First, the separation point is found not to change much with the angle of attack. Secondly, the separation point moves upstream (relative to the separation point for $\alpha = 0$) at low angle of attack (say $\alpha < 8°$ for $b/a = \frac{1}{4}$) but reverses this trend to move downstream instead at large angle of attack (say $\alpha > 8°$ for $b/a = \frac{1}{4}$). This unusual behaviour is attributed, of course, to the downstream flow becoming less and less boundary-layer-like as the angle of attack increases.

Figure 7 (*f*) gives the displacement thickness. What is unusual here is that the displacement thickness does not always increase monotonically in the downstream direction except at low angle of attack (say $\alpha = 3° \sim 6°$). At larger angle of attack, the displacement thickness first goes up and then may go down despite the continuing rapid increase of the outer edge distance. This result follows from the fact that the integrated u-velocity defect does not increase with the increase of the outer edge distance, because the u-velocity profiles are nearly flat as shown in figure 7 (*c*). (Note that calculation for $\alpha = 31{\cdot}87°$ has not been carried out to the separation point.)

5. Discussion

Having presented the results obtained, we turn to elaborate some of the implications and consequences regarding the flow pattern and the question of separation.

Significance of the S-shaped $\partial v/\partial\theta$ profile

From the derivative $\partial v/\partial\theta$ at the symmetry plane, one obtains the velocity v according to

$$v = \Delta\theta(\partial v/\partial\theta)_{\text{sym. plane}},$$

at some angle $\Delta\theta$ off the symmetry plane. Thus the S-shaped profile of $\partial v/\partial\theta$ at the symmetry plane implies an S-shaped profile of v on both sides near the symmetry plane (figure 8). Such a profile suggests in turn the formation of streamwise vortices† inside the boundary layer in contrast to the crosswise vortices which are familiar in two-dimensional boundary layers.

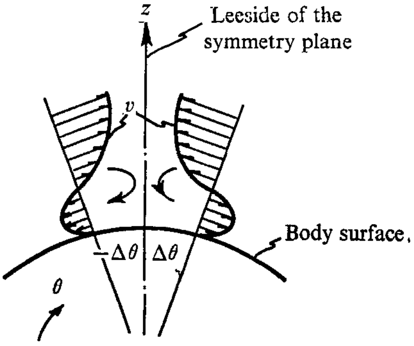

FIGURE 8. S-shaped v-velocity profile.

Analogous to the separation point determined by $(\partial u/\partial z)_{z=0} = 0$, the point which marks the beginning of the presence of an embedded vortex is determined by

$$\left[\frac{\partial}{\partial z}\left(\frac{\partial v}{\partial \theta}\right)_{\theta=0,\pi}\right]_{z=0} = 0.$$

Assuming that v depends continuously on z and θ as it should for a smooth flow, one can exchange the order of differentiation

$$\left[\frac{\partial}{\partial z}\left(\frac{\partial v}{\partial \theta}\right)_{\theta=0,\pi}\right]_{z=0} = \left[\frac{\partial}{\partial \theta}\left(\frac{\partial v}{\partial z}\right)_{z=0}\right]_{\theta=0,\pi} = 0.$$

Hence the vortex starting point on the symmetry plane may be further identified as the point (on the symmetry plane) at which the lateral derivative of the cross skin friction, $C_{f\theta}$, vanishes. Immediately ahead and after this point along the streamwise direction, $\partial(C_{f\theta})/\partial\theta$ takes opposite signs. The fact that the separation point and the vortex starting point are two distinct points has important impact

---

† The idea of the formation of streamwise vortices is largely taken from the literature. Actually, whether such circulating vortices really exist and if so in what form (spiral?) remain to be proved.

on the current understanding of the flow pattern and the three-dimensional separation to be discussed later.

The preceding results reveal that the embedded vortices are present on both the windside and leeside. On the windside, the vortex appears only in a short streamwise interval immediately ahead of the (streamwise) separation point; and it extends in the normal direction only a fraction of the whole boundary-layer thickness. On the leeside, the vortex appears much earlier in the streamwise direction and may even extend over the entire leeside depending on the angle of attack. Meanwhile the leeside vortex may extend across the entire boundary-layer thickness.

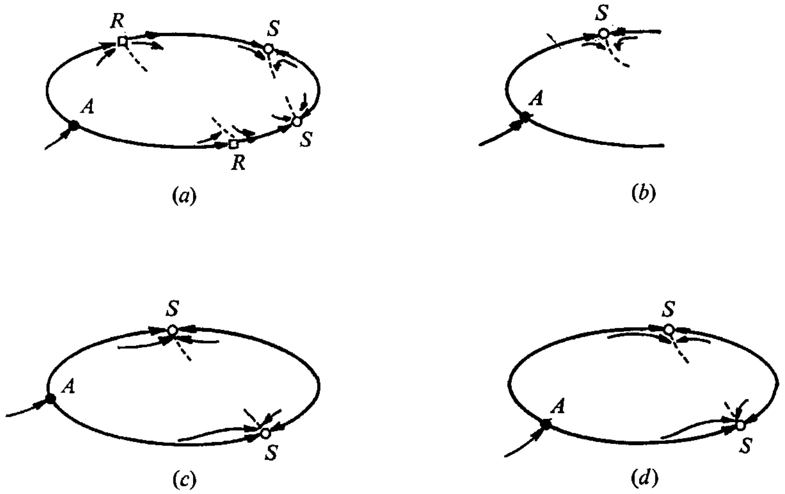

(a) (b) (c) (d)

FIGURE 9. Flow pattern near the symmetry plane. A is the attachment point, S the separation point and R the vortex starting point. (*a*) Present. (*b*) Maskell. (*c*) Low incidence. (*d*) High incidence. (*c*) and (*d*) Cooke & Brebner, also Eichelbrenner.

Flow pattern

On the basis of our present results, the flow pattern near the symmetry plane is sketched in figure 9(*a*). Let us just focus our discussion on the leeside. Adjacent to the symmetry plane, the direction of v velocity close to the body surface is reversed near the vortex starting point R, while the u-velocity direction remains unchanged until the separation point S. Consequently, the limiting streamline ahead of R is directed towards the symmetry plane, while that downstream of R is directed away from the symmetry plane. Behind the point S, since the u velocity close to the wall is also reversed, the limiting streamline points upstream and at the same time away from the symmetry plane.

Compared to the flow ahead of R, one may speak of the flow between R and S as partially reversed (i.e. v-velocity reversal only), while the flow behind S as completely reversed (i.e. both u and v velocity are reversed).

The flow pattern just described differs from what has been described, for example, in the works of Maskell (1955), Cooke & Brebner (1961) and Eichelbrenner (1957). These authors sketched more complete limiting streamline patterns over the body surface; the portions near the symmetry plane are re-sketched in figures 9(*b*), (*c*), (*d*) for the purpose of comparison here. The main difference between the present work and those cited is the omission of the point R in the latter. Figure 9(*d*) for $\alpha \geqslant 9^\circ$ does imply reversal of v velocity ahead of S and hence seems to be in agreement with figure 9(*a*). However, figure 9(*c*) for $\alpha \leqslant 9^\circ$ shows an opposite trend on the leeside which was not found in the present work.

We have so far deliberately avoided any inferences regarding the flow farther away from the symmetry plane because the present solutions are invalid there. However, knowing the symmetry-plane solutions on both the windside and the leeside, one does gain a fairly good idea concerning the general flow trend over an entire body even though much of the detail is lacking. This is one of the reasons which makes such symmetry-plane calculations important.

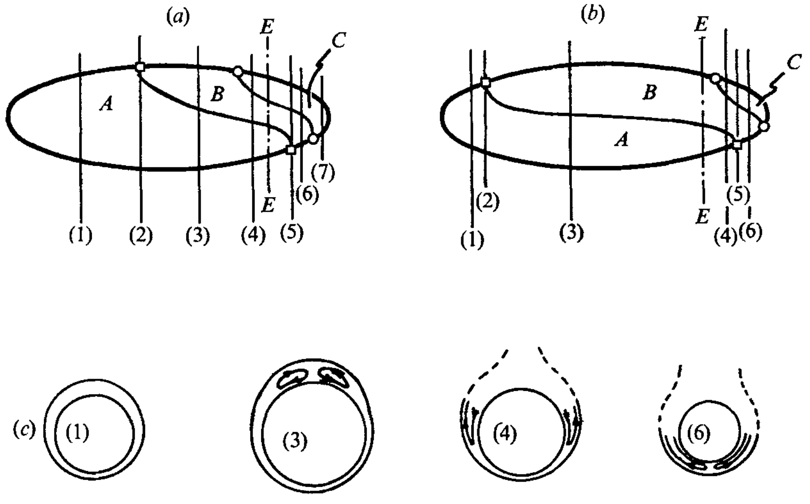

FIGURE 10. Sketch of general flow pattern. (*a*) Low angle of attack. (*b*) High angle of attack. ○, separation; ☐, start of vortex; *E*— · —*E*, separation line for axisymmetrical case; – – –, undeterminable by boundary-layer equations.

In the axially symmetrical case, the flow separates along a parallel (as shown by line *EE* in figures 10(*a*), (*b*). As the angle of attack increases, embedded vortices start to emerge. If we connect the vortex starting points and the separation points on the wind- and leeside, the flow is divided into three regions (figures 10(*a*), (*b*), the regular boundary-layer region *A*, the embedded vortex region *B* and the separated region *C*. For later convenience of reference, let us refer to these connecting curves as the vortex starting line and the separation line respectively. The precise nature of these curves remains to be defined. But on the basis of our present results, there are two such curves which divide the boundary layer into three distinct regions. In the literature including the works of Maskell (1953), Cooke & Brebner (1961), and Eichelbrenner (1957), the intermediate region *B* was not singled out.

Cross-sectional sketches (figure 10(c)) further illustrate gradual development of the boundary layer. Station (1) at the front shows a regular boundary layer all round, slightly thinner on the windside. At station (3), embedded vortices appear on the leeside, but the boundary layer remains thin and unseparated, at least, at low incidence. At station (4) further down the stream, separation occurs at the top. At station (6), separation becomes more pronounced and the embedded vortices extend to the bottom. Station (7) falls completely in the separated region. At stations (4) and (6), we have left the outer edge open on the top to indicate that the solutions there are beyond determination by boundary-layer theory. This does not necessarily imply an infinite wake behind.

At low angle of attack, region B is thin and the vortex is embedded inside the boundary layer. At larger angle of attack, region B is not thin; the vortices grow to large size, and basic concepts for a thin boundary layer are however no longer valid. Furthermore, contrary to usual expectation, the separation point moves downstream instead of upstream. Under this circumstance, the 'separation line' referred to so far seems to have lost its meaning. It would make more sense to redesignate the vortex starting line as the separation line. This raises a fundamental question on how the three-dimensional separation should be defined.

Perhaps a word of caution is in order at this point. The present work follows strictly the classical boundary-layer theory with the pressure given by the inviscid solution, but this is known to be inaccurate when the boundary layer is not thin enough. The results, therefore, would be certainly somewhat modified if a more realistic pressure distribution, say from experiments, were used.

Separation

The definition of three-dimensional separation has long been an unsettled question (Brown & Stewartson 1969). There are several versions yet none seems to be undisputedly accepted.

Maskell (1955), for example, sketched a bubble separation upon a body of revolution at incidence. He defined the envelope of limiting streamlines as the separation line with a singular point in the plane of symmetry. By singular, it is meant that the components of skin friction all vanish. This is the same definition we have used for the separation point on the symmetry plane. On the other hand, Lighthill (1963) defined the separation line as 'a skin friction line (or limiting streamline) which issues from both sides of a saddle point of separation and, after embracing the body, disappears into a nodal point of separation'. Referring to our present problem, the saddle point and nodal point of separation are just the separation points determined on the windside and leeside of the symmetry plane. Both Maskell and Lighthill, therefore, assert that the separation line passes through the separation points (based on the vanishing skin friction) on the symmetry plane, though they differ as to whether the separation line is the envelope of limiting streamlines or is itself also a limiting streamline.

We cannot comment on their difference because this would require more complete solutions off the symmetry plane. But we disagree with their common assertion that the separation line passes through the singular points (S in figure 9(*a*)) on the symmetry plane. Instead we maintain on the basis of our present results that at larger angle of attack (say $\alpha > 8^\circ$ for $b/a = \frac{1}{4}$), the region B should be more appropriately referred to as 'separated' and hence the separation would occur ahead of S. In this respect we also disagree with Cooke & Brebner (1961) and Eichelbrenner (1957). As shown in figure 9(*c*), (*d*), these latter authors also show that the separation line passes through the singular points, S, on the symmetry plane.

At least near the symmetry plane, the separation, which we maintain occurs ahead of S, can be clearly identified as cross-flow separation (i.e. due to reversal of v velocity). For the type of flow considered, such cross-flow separation occurs much earlier than the streamwise separation which does not occur until the point S. Previous investigators seemed to have attached too much emphasis on the streamwise separation and hence have considered without exception (at least to the author's knowledge) that the separation line passes through the points, S, on the symmetry plane. Actually the cross-flow separation is more intuitively obvious in the flow over an inclined body. In fact the best known solution for this type of flow is the supersonic cone problem of Moore (1953) where the separation is entirely crosswise (i.e. in the circumferential direction).

We have so far restricted our comments on the flow separation to near the symmetry plane and emphasized the phenomena of the cross-separation. Away from the symmetry plane, the terms 'cross' and 'streamwise' become vague, and the problem is beyond the scope of the present work. Before concluding, we may mention that Moore (1953) also suggested a different version of separation. He tried to identify the separation with the existence of a bubble of fluid embedded in the boundary layer. In a qualitative way, this version of the separation line seems to have some relevance with the starting vortex line referred to in the present work. However, it is difficult at this moment to demonstrate such relevance more clearly, since neither the vortex starting line used here nor Moore's bubble edge is precisely defined despite such a bubble being physically easy to identify.

The author is indebted to Dr S. H. Maslen for his discussions and to Mrs Barbara Hawkins for programming and obtaining the numerical solutions.

Appendix A. Difference equations

With the quotient approximations of (8*a*, *b*, *c*), the difference form of (5*b*) becomes (remembering all the coefficients of derivatives are evaluated at $(l+\frac{1}{2}, n)$)

$$a_{1n} u_{l+1,n-1} + b_{1n} u_{l+1,n} + c_{1n} u_{l+1,n+1} = d_{1n}, \tag{A 1}$$

where

$$a_{1n} = \frac{-w_{l+\frac{1}{2},n}}{4\Delta z} - \frac{1}{2(\Delta z)^2} = -c_{1n}, \tag{A 1a}$$

$$b_{1n} = \frac{u_{l+\frac{1}{2},n}}{(h_\mu)_{l+\frac{1}{2}}\Delta\mu} + \frac{1}{(\Delta z)^2}, \tag{A 1b}$$

$$d_{1n} = a_{1n} u_{l,n+1} + \left(\frac{u_{l+\frac{1}{2},n}}{(h_\mu)_{l+\frac{1}{2}}\Delta\mu} - \frac{1}{(\Delta z)^2}\right) u_{l,n} - a_{1n} u_{l,n-1} - \left(\frac{\partial p}{h_\mu \partial\mu}\right)_{l+\frac{1}{2}}. \tag{A 1c}$$

The difference form of $(5c)$ becomes

$$a_{2n}\left(\frac{\partial v}{\partial \theta}\right)_{l+1,\,n-1}+b_{2n}\left(\frac{\partial v}{\partial \theta}\right)_{l+1,\,n}+c_{2n}\left(\frac{\partial v}{\partial \theta}\right)_{l+1,\,n+1}=d_{2n}, \tag{A 2}$$

where

$$a_{2n}=r_{l+\frac{1}{2}}a_{1n}=-r_{l+\frac{1}{2}}c_{2n}, \tag{A 2a}$$

$$b_{2n}=\left(\frac{r}{h_\mu}\right)_{l+\frac{1}{2}}\frac{u_{l+\frac{1}{2},\,n}}{\Delta\mu}+\frac{1}{2}\left(\frac{\partial v}{\partial \theta}\right)_{l+\frac{1}{2},\,n}+\frac{1}{2}\left(\frac{\partial r}{h_\mu\,\partial\mu}\right)_{l+\frac{1}{2}}u_{l+\frac{1}{2},\,n}+\frac{r_{l+\frac{1}{2}}}{(\Delta z)^2}, \tag{A 2b}$$

$$\begin{aligned}d_{2n}=&-c_{2n}\left(\frac{\partial v}{\partial \theta}\right)_{l,\,n+1}+\left[\left(\frac{r}{h_\mu}\right)_{l+\frac{1}{2}}\frac{u_{l+\frac{1}{2},\,n}}{\Delta\mu}-\frac{1}{2}\left(\frac{\partial v}{\partial \theta}\right)_{l+\frac{1}{2},\,n}\right.\\&\left.-\frac{1}{2}\left(\frac{\partial r}{h_\mu\,\partial\mu}\right)_{l+\frac{1}{2}}u_{l+\frac{1}{2},\,n}-\frac{r_{l+\frac{1}{2}}}{(\Delta z)^2}\right]\left(\frac{\partial v}{\partial \theta}\right)_{l,\,n}-a_{2n}\left(\frac{\partial v}{\partial \theta}\right)_{l,\,n-1}-\left(\frac{\partial^2 p}{\partial \theta^2}\right)_{l+\frac{1}{2}}.\end{aligned} \tag{A 2c}$$

The difference continuity equation from $(10a,\, b)$ and $(5a)$ is

$$w_{l+\frac{1}{2},n}=w_{l+\frac{1}{2},n-1}-d_{3n}, \tag{A 3}$$

where

$$\begin{aligned}d_{3n}=\frac{\Delta z}{r_{l+\frac{1}{2}}}\Bigg\{&\left[\left(\frac{r}{h_\mu}\right)_{l+\frac{1}{2}}\frac{1}{2\Delta\mu}+\frac{1}{4}\left(\frac{\partial r}{h_\mu\,\partial\mu}\right)_{l+\frac{1}{2}}\right](u_{l+1,\,n}+u_{l+1,\,n-1})\\&+\left[-\left(\frac{r}{h_\mu}\right)_{l+\frac{1}{2}}\frac{1}{2\Delta\mu}+\frac{1}{4}\left(\frac{\partial r}{h_\mu\,\partial\mu}\right)_{l+\frac{1}{2}}\right](u_{l,\,n}+u_{l,\,n-1})\\&+\frac{1}{4}\left[\left(\frac{\partial v}{\partial \theta}\right)_{l+1,\,n}+\left(\frac{\partial v}{\partial \theta}\right)_{l,\,n}+\left(\frac{\partial v}{\partial \theta}\right)_{l+1,\,n-1}+\left(\frac{\partial v}{\partial \theta}\right)_{,\,n-1}\right]\Bigg\}.\end{aligned} \tag{A 3a}$$

Appendix B. Initial values

The initial values used for starting the present calculation were obtained from the stagnation point solution of Squire (1965). Squire extended Howarth's (1951) work on the stagnation-point boundary layer over a general curvilinear three-dimensional surface to include next higher order terms in the series expansion. Specialized to our present use, Squire's solutions appear as:

$$u=b_1g_0'(\bar{z})\,(h_\mu)_0(\mu-\mu_0)+[b_{22}g_{34}'(\bar{z})+a_1c_2g_{32}'(\bar{z})+a_1d_2g_{33}'(\bar{z})]\,[(h_\mu)_0(\mu-\mu_0)]^2, \tag{B 1}$$

$$\partial v/\partial\theta=(h_\theta)_0\{a_1f_0'(\bar{z})+[a_1c_2f_{22}'(\bar{z})+a_1d_2f_{23}'(\bar{z})+b_{22}f_{24}'(\bar{z})]\,(h_\mu)_0(\mu-\mu_0)\}, \tag{B 2}$$

where

$$a_1=\frac{(1+k_c)\sin\alpha}{(h_\theta)_0},\quad \bar{z}=a_1^{\frac{1}{2}}z, \tag{B 3a,b}$$

$$b_1=\frac{b}{a}\,\frac{(1+k_c)\sin\alpha}{(h_\mu)_0(1-\mu_0^2)\,(1-e^2\mu_0^2)}, \tag{B 3c}$$

$$b_{22}=\frac{1}{2}\,\frac{b}{a}\,\frac{(\sin\alpha)\,(1+k_c)\,\mu_0(1-3e^2\mu_0^2+2e^2)}{(1-e^2\mu_0^2)^{\frac{5}{2}}\,(1-\mu_0^2)}, \tag{B 3d}$$

$$c_2=\frac{-\mu_0}{(1-\mu_0^2)^{\frac{1}{2}}\,(1-e^2\mu_0^2)^{\frac{1}{2}}},\quad d_2=\frac{\mu_0(1-e^2)}{(1-\mu_0^2)^{\frac{1}{2}}\,(1-e^2\mu_0^2)^{\frac{3}{2}}}. \tag{B 3e,f}$$

The subscript zero indicates the quantities evaluated at the stagnation point. Functions f_0 and g_0 are determined by Howarth's equations (12–13), functions f_{2i} and g_{3i} $(i = 1, 2, 3)$ are determined by Squire's equation (45). Howarth and Squire solved these functions for a few cases; we have solved these functions for a number of specified values of the angle of attack α and the thickness ratio $b/a = \frac{1}{4}$.

REFERENCES

Brown, S. N. & Stewartson, K. 1969 In *Annual Review of Fluid Mechanics*, **1** (ed. W. R. Sears and M. Van Dyke).

Cooke, J. C. & Brebner, G. G. 1961 *Boundary Layer and Flow Control*, Vol. 1. (Ed. G. V. Lachmann.) New York: Pergamon.

Eichelbrenner, E. A. 1957 *O.N.E.R.A. Publication* no. 89.

Eichelbrenner, E. A. & Ondurt, A. 1955 *O.N.E.R.A. Publication* no. 76.

Flügge-Lotz, I. & Blottner, F. G. 1963 *J. de Mecanique*, II, 4.

Forsyth, G. E. & Wasow, W. R. 1960 *Finite-Difference Methods for Partial Difference Equations.* New York: Wiley.

Howarth, L. 1951 *Phil. Mag.* (7) **42**, 1433.

Lamb, H. 1932 *Hydrodynamics.* Cambridge University Press.

Lighthill, M. J. 1963 In *Laminar Boundary Layers.* (Ed. L. Rosenhead.) Oxford University Press.

Martin, J. C. & Gerber, N. 1957 *BRL Rep.* 1038, *Aberdeen Proving Ground, Md.*

Maskell, E. C. 1955 *RAE Rep.* no. Aero. 2565.

Moore, F. K. 1952 *NACA TN* 2844.

Moore, F. K. 1953 *J. Aero. Sci.* **20**, 525–534.

Nonweiler, T. 1955 In *Incompressible Aerodynamics.* (Ed. B. Thwaites.) Oxford University Press.

Schlichting, H. 1955 *Boundary Layer Theory.* New York: McGraw Hill.

Smith, A. M. O. & Clutter, D. W. 1963 *A.I.A.A. J.* **1**, 9.

Squire, L. C. 1955 *Aero. Res. Counc. R & M*, no. 3006.

Trella, M. & Libby, P. A. 1965 *A.I.A.A. J.* **3**, 1.